


Temperature Measurement of Laser-Irradiated Metals Using Hyperspectral Imaging

Dong-Xia Qu, Joel Berry, Nicholas P. Calta, Michael F. Crumb, Gabe Guss, and Manyalibo J. Matthews*

Lawrence Livermore National Laboratory, Livermore, California 94550, USA

 (Received 15 March 2020; revised 23 June 2020; accepted 25 June 2020; published 10 July 2020)

Accurate noncontact surface-temperature measurements during laser-based materials processing remain challenging due to the difficulty of establishing reliable emissivity values as a function of temperature and wavelength. Direct measurement of emissivity is difficult, as the emissivity may be changing constantly in the laser-material interaction region, where the temperature gradients are extreme and surface displacement can complicate the measurement. Here, we present a hyperspectral imaging method using a multiwavelength camera to capture the spectral radiance in eight different bands and fit the wavelength-dependent radiance to Planck's law. Time-resolved temperature measurements during microsecond pulsed-laser irradiation of a metal plate made of the titanium alloy Ti-6Al-4V provide temperature information about the irradiated surface with an estimated accuracy of $\pm 10\%$. The extracted wavelength-dependent emissivity slope compares well with reported results for macroscale titanium melts obtained using IR spectroscopy, which measure temperature without any built-in assumptions about the emissivity. The results are directly applicable to temperature monitoring during welding, additive manufacturing, and semiconductor growth.

DOI: [10.1103/PhysRevApplied.14.014031](https://doi.org/10.1103/PhysRevApplied.14.014031)

I. INTRODUCTION

Laser-based materials processing is continuing to attract great interest and is finding fast-growing applications in many fields, such as in the aeronautics, space, automotive, nuclear-fusion, and tooling industries [1–3]. Examples include the production of fan blades and fuel nozzles by additive manufacturing (AM) for General Electric jet engines, the production of cooling ducts for the auto-racing industry, and the manufacture of dental copings for dental crowns and bridges. AM systems hold the promise of producing defect-free and cost-effective complex metal parts that cannot be easily manufactured using conventional methods. However, complicated thermal histories during laser-metal interaction can lead to problematic areas and abnormal microstructures [4–8]. Therefore, measurements of the temperature distribution in the metallic melt pool during the laser-melting process are of vital importance [9], because they provide valuable input about the cooling rates and thermal histories necessary to determine microstructure evolution and material properties via fundamental multiphysics models.

Over the past three decades, a significant amount of effort has been put into the development of noncontact temperature-monitoring systems to obtain accurate temperature profiles during laser-metal interactions and

solid-liquid phase transitions [10,11]. Pyrometry is an effective optical technique that measures the temperature of an object based on the wavelengths and amounts of electromagnetic energy that the object radiates in thermal equilibrium. State-of-the-art pyrometry methods detect the emitted radiance at multiple wavelengths, ranging from two colors to hundreds of colors, to address the difficulty of unknown emissivity [12–17]. Both multiple-camera systems and single moving hyperspectral line cameras have been used in melt-pool temperature measurements during laser-material interaction processes [16,18]. However, the temperature accuracy of multiple-camera-based systems is limited by the fact that they capture the spectral radiance at a small number of wavelengths; e.g., in a two-color system, one has to assume that the emissivity ratio between two different wavelengths is invariant with respect to temperature. On the other hand, the hyperspectral-line-camera-based method can measure the thermal emission at hundreds of spectral points and extract the absolute temperature [18]. However, this method can obtain real-time temperature profiles along only one axis.

In this study, we employ a hyperspectral camera to obtain the two-dimensional (2D) spectral radiance at eight different wavelengths and extract the temperature distribution by fitting the measured spectra according to Wien's approximation. Our approach differs from that of other studies in both the compact method used for filtering wavelength bands and the relatively large number of bands

*matthews11@llnl.gov

used, which improves accuracy. This technique enables temporally and spatially resolved temperature measurements that allow the inclusion of effects of spectrally and spatially varying emissivity in the melt pool. Our system is able to capture a real-time 2D image without the need to move the camera. We determine the temperature value in each pixel group considered by approximating the spectral emissivity as a linear function of wavelength.

This paper is organized as follows. In Sec. II, the experimental setup and the details of the hyperspectral camera are described. We then introduce the theoretical background, present the procedure used to calibrate the hyperspectral camera, and discuss the data-analysis method in Sec. III. This is followed by a presentation and discussion of the experimental results on laser heating and melting of Ti-6Al-4V metal plates in an argon atmosphere in Sec. IV. A comparison of the emissivity obtained here and a value obtained by a different experimental technique is presented. In Sec. V, we present the thermal modeling of pulsed-laser-heated Ti-6Al-4V and compare the results with our experiments. Finally, the paper is summarized in Sec. VI.

II. EXPERIMENTAL SETUP

Figure 1(a) shows a schematic illustration of the experimental setup. We illuminate the surface of a bare Ti-6Al-4V metal plate in an open space using a JK Yb-fiber laser (model JK600FL) operating at 1070 nm in a quasicontinuous mode with an operation frequency of 1 kHz and a pulse width of 0.8–30 μs . The laser beam is focused down to a 50- μm - $1/e^2$ -diameter Gaussian shape with a peak laser power of approximately 220 W. The laser beam size and peak power are similar to those used in laser

powder-bed fusion processes. However, since the beam is stationary in our study, modulation is used to “mimic” transient effects resulting from scanning and allow heat to diffuse away between pulses. Importantly, by using this modified process we are able to achieve peak temperatures within the ranges relevant to laser welding and laser powder-bed fusion. The average power is reduced using modulation to values below 6.6 W. In future work, a laser scanning system (with a speed of 1 m/s) will be incorporated, but this demands the use of an imaging system with at least a 50-kHz frame rate to capture the relevant melt-pool dynamics [9,25,31,32].

Pure argon gas flows continuously at approximately 5000 sccm over the sample surface to prevent oxidation during the laser heating and melting. The emitted spectral radiance is directed by a long-pass dichroic filter (cutoff wavelength 900 nm) to a microscope (NA 0.21, working distance 64 mm, $9 \times$ magnification). A notch filter with a short-pass edge at 850 nm and an absorptive neutral-density filter (optical density 0.4) are placed in front of the microscope to block scattered laser light and attenuate thermal emission. We capture the spectral images using a hyperspectral camera (model Silios CMS-V) with 1280×1024 pixels. Each square pixel is $5.3 \times 5.3 \mu\text{m}^2$ in area. The hyperspectral camera is made of a CMOS image sensor with a matrix filter. The matrix filter is based on macropixels that integrate eight color band-pass filters ranging from 544 to 815 nm and one panchromatic (white-light) filter, arranged in a 3×3 matrix [Fig. 1(b)]. The overall area of such a group of 3×3 pixels is $15.9 \times 15.9 \mu\text{m}^2$. A black-body system (Infrared Systems Development IR-563/301) with a maximum operating temperature of 1473 K is employed to calibrate our hyperspectral camera.

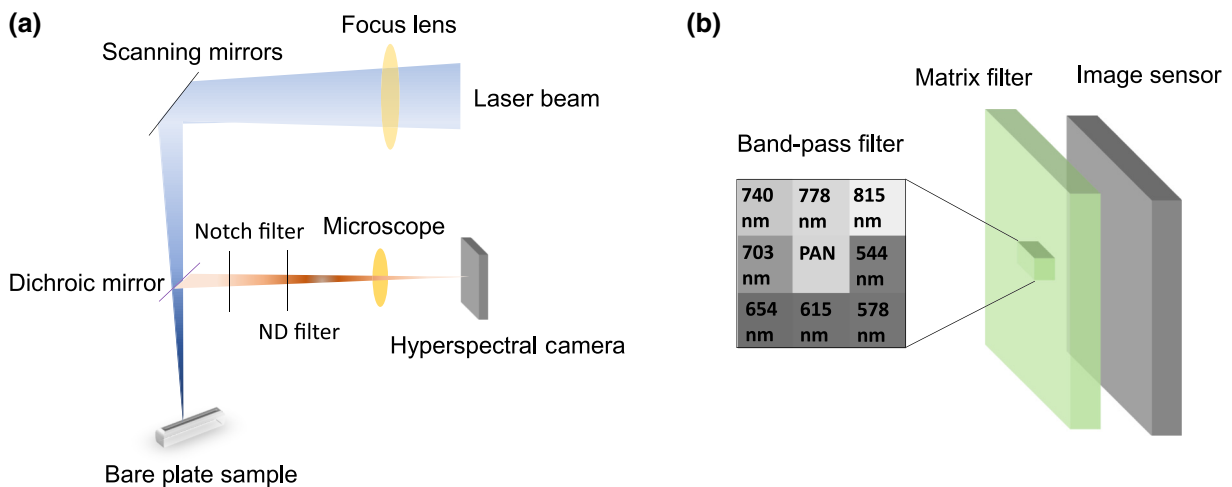


FIG. 1. (a) Schematic illustration of the experimental setup, monitored with a hyperspectral-camera system. ND, neutral density. (b) Side view of the filter arrangement in the hyperspectral camera. PAN, panchromatic.

III. CALIBRATION AND CALCULATION METHOD

A. Theoretical model

Based on Planck's law, the radiance I emitted by an object is a function of the wavelength λ and temperature T , viz.

$$I(\lambda, T) = \varepsilon(\lambda, T) \frac{2hc^2}{\lambda^5} \left[\exp\left(\frac{hc}{\lambda k_B T}\right) - 1 \right]^{-1}, \quad (1)$$

where $\varepsilon(\lambda, T)$ is the wavelength- and temperature-dependent emissivity, h is Planck's constant, c is the speed of light, k_B is Boltzmann's constant, and T is the absolute temperature. In order to find the temperature of an object with an unknown emissivity via its spectral radiance, it is important to establish a reliable emissivity model that can correctly approximate the object's spectral emissivity.

The temperature of an object can be determined from a least-squares fit of Eq. (1) to the experimental data. In general, the least-squares minimization problem for a multiwavelength imaging pyrometer can be expressed as

$$\min_{T, \varepsilon} \chi^2 = \min_{T, \varepsilon} \sum_{i=1}^N \left\{ \frac{[S_i - S_i(T, \varepsilon, \lambda)]^2}{\sigma_i^2} \right\} \rightarrow T, \varepsilon(\lambda, T), \quad (2)$$

where S_i is the detected signal at λ_i , $S_i(T, \varepsilon, \lambda)$ is the theoretical signal at λ , T is the unknown temperature of the target, $\varepsilon(\lambda)$ is the emissivity model, and σ_i is the root-mean-square value of the noise in the signal, which is the square root of the standard error. Previous emissivity measurements on various materials have shown that the spectral emissivity can be represented by a second-order polynomial function of the wavelength for metals [19]:

$$\varepsilon(\lambda) = a_0 + a_1\lambda + a_2\lambda^2 + \dots, \quad (3)$$

where a_0, a_1, a_2, \dots are the parameters of the emissivity model.

It has been shown that the spectral emissivity of liquid pure Ti metal can be adequately approximated as a linearly decreasing function of wavelength [20]. Hence, we use a general spectral-emissivity model given by

$$\varepsilon(\lambda_i) = B - A \frac{\lambda_i - \lambda_1}{\lambda_8 - \lambda_1} \quad (0 \leq A < B \leq 1, i = 1, \dots, 8), \quad (4)$$

where λ_i ($i = 1, \dots, 8$) represents the i th wavelength at which the spectral radiance is measured, A and B are constants constrained between 0 and 1, and $\varepsilon_{\text{ave}} = B - A/2$ is the average emissivity over the region λ_1 – λ_8 . The application of Eq. (4) to Eq. (2) results in fitting parameters A, B , and T for a least-squares fit of Eq. (2).

B. 2D eight-band pyrometry

By using a hyperspectral camera where finely resolved spectral information is provided for each pixel, we are able to measure the spectral radiance of the heated surface at eight distinct wavelengths, i.e., 544, 578, 615, 654, 703, 740, 778, and 815 nm, with a full width at half maximum of 41, 42, 37, 40, 37, 38, 44, and 40 nm, respectively. In order to confirm that our technique can accurately determine the temperature of the target, we first take an image of a black-body source cavity set at $T = 1473$ K, as illustrated in the inset of Fig. 2. An enlarged view of a 3×3 macropixel is shown in the inset, where channels 1–8 are color-filtered, whereas channel 9 is panchromatic.

Figure 2 shows the measured radiance in the eight channels after taking into account the quantum efficiency of the camera in the eight bands, as well as the wavelength-dependent transmission coefficient of the microscope, the neutral-density filter, the notch filter, and the dichroic mirror. In this case, a constant emissivity yields the best fit because of the black-body nature of the cavity. Using Eqs. (1) and (2), we achieve a good fit (red curve), as shown in Fig. 2. The packages MATLAB™ and OriginLab™ are used to carry out the nonlinear least-squares calculations and generate consistent results. The temperature identified is $T = 1528 \pm 31$ K, fairly close to the real black-body-source temperature, $T = 1473 \pm 10$ K. The 3% discrepancy may come from the finite bandwidth of each

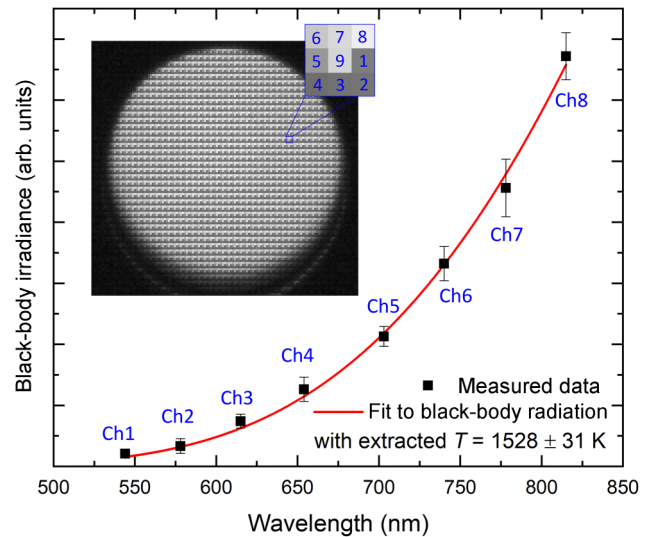


FIG. 2. Spectral radiance measured by the hyperspectral camera when imaging a known black-body source cavity at a temperature of 1473 K. The experimental data fit well with the prediction based on Planck's law for black-body radiation. Inset: raw image of the black-body source cavity; this image consists of a matrix made up of groups of 3×3 spectral-band-filtered pixels called macropixels. An enlarged view of the nine interleaved pixels in a macropixel is shown in the top right corner.

spectral channel, but nevertheless the small discrepancy demonstrates the effectiveness of our method.

IV. RESULTS

A. Spectral image

We start by taking a snapshot of the irradiated surface after approximately 2 s of pulsed heating (Fig. 3, bottom panel). The exposure time for image collection is 7.66 ms to avoid saturating the CMOS image sensor. The image shown in Fig. 3 is captured by use of channel 9, with a spatial resolution of $15.9 \mu\text{m}/\text{macropixel}$ along with a magnification of approximately 9. The intensity profile closely resembles a Gaussian distribution (Fig. 3, right panel).

The raw images taken simultaneously in the other eight different bands in the same set of captured thermal emission data are shown in the insets in Fig. 4. The kurtosis and skewness of the line profiles of the thermal images are quite different for different channels (Fig. 4). For example, channels 1–4 display a lower kurtosis than do channels 5–8. The skewness of channel 1 is almost 3 times larger than that of channel 6. We also confirm that the observed skewness and kurtosis are due to the real heated spot, rather

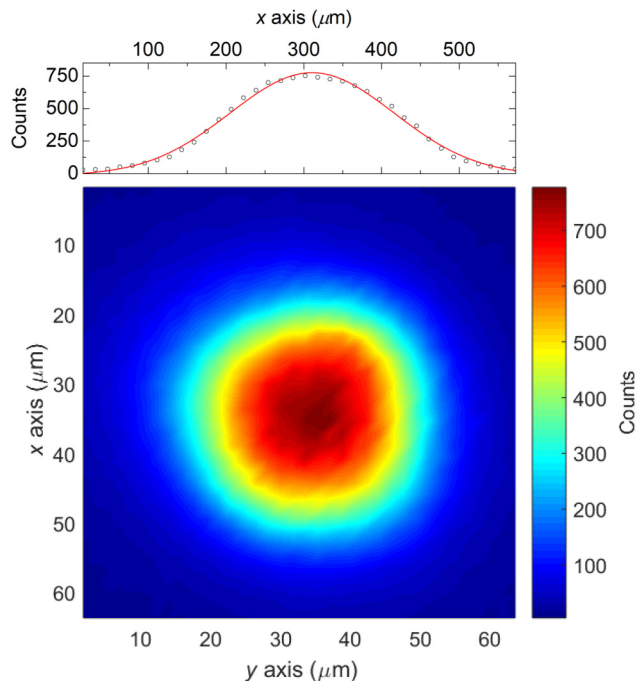


FIG. 3. Top panel: line profile of camera pixel counts (black circles) along x axis at the center of the broadband image shown in the bottom panel. The red line shows a fit to a Gaussian function. Bottom panel: snapshot of a broadband thermal image of a laser-irradiated Ti-6Al-4V surface. The color bar represents the measured pixel counts from the hyperspectral camera.

than to nonuniform pixels in the camera. The channel-dependent skewness and kurtosis indicate that the thermal emission indeed displays a wavelength dependence, which may be correlated with the wavelength-dependent emissivity shown in Fig. 8.

B. Snapshot of temperature and emissivity profile

While the surface of the Ti-6Al-4V plate is irradiated with the focused laser beam, the emitted light is measured to allow us to calculate the temperature at every micropixel according to the procedure outlined in Sec. III. A contour plot of a single-shot 2D temperature profile is illustrated in Fig. 5, in which each contour line is labeled with its associated temperature value. We find that the measured temperature decreases monotonically from the center of the heated region, in contrast to a temperature profile incorrectly extracted near the liquidus-solidus region [21] in a previous report on the hyperspectral-line-camera method [18]. Figure 6 shows the corresponding standard error in the temperature. In the high-temperature region ($T > 2200$ K), the standard error is in the range of 100–300 K, whereas in the low-temperature region ($T \leq 2200$ K), the standard error is below 50 K. Therefore we estimate that the upper bound on the standard error in the temperature is generally below 10%. We attribute the general increase in the standard error above approximately 2200 K to increased liquid-phase volatility and increased vapor-phase contributions after many pulse cycles, as well as to transient thermal effects from irregularities in the shape of the surface crater drilled by the laser beam over time. We also associate these surface-shape irregularities with the presence of small localized temperature variations in the central high-temperature region in Fig. 5. Our analysis indicates that these localized variations are physical (the data can be fitted by Planck’s law). Since a liquid melt pool is expected to exist only during a small fraction of each pulse cycle (see Sec. V), and the imaging time encompasses nearly 17 cycles, melt-pool fluid-flow effects such as flow instabilities are unlikely to contribute directly to these variations. In contrast, solid-phase surface-shape irregularities can be sustained more readily over the imaging time, with subsequent thermal signatures (local focusing or scattering) surviving in the time-averaged data. However, the magnitudes of the observed variations are relatively small.

A 2D profile of the relative average emissivity ε_{ave} is plotted in Fig. 7. Because the absolute magnitude of the emissivity is not measured using our hyperspectral system, we assume that the average emissivity is 0.12 at $T = 2200$ K [20] and scale the emissivity at other temperatures by the ratio of the extracted emissivity to the emissivity at $T = 2200$ K. In the center of the irradiated region, the average emissivity is almost constant, such that $\varepsilon_{\text{ave}} \approx 0.04$ for $T > 2600$ K. Just outside the center, ε_{ave} quickly increases

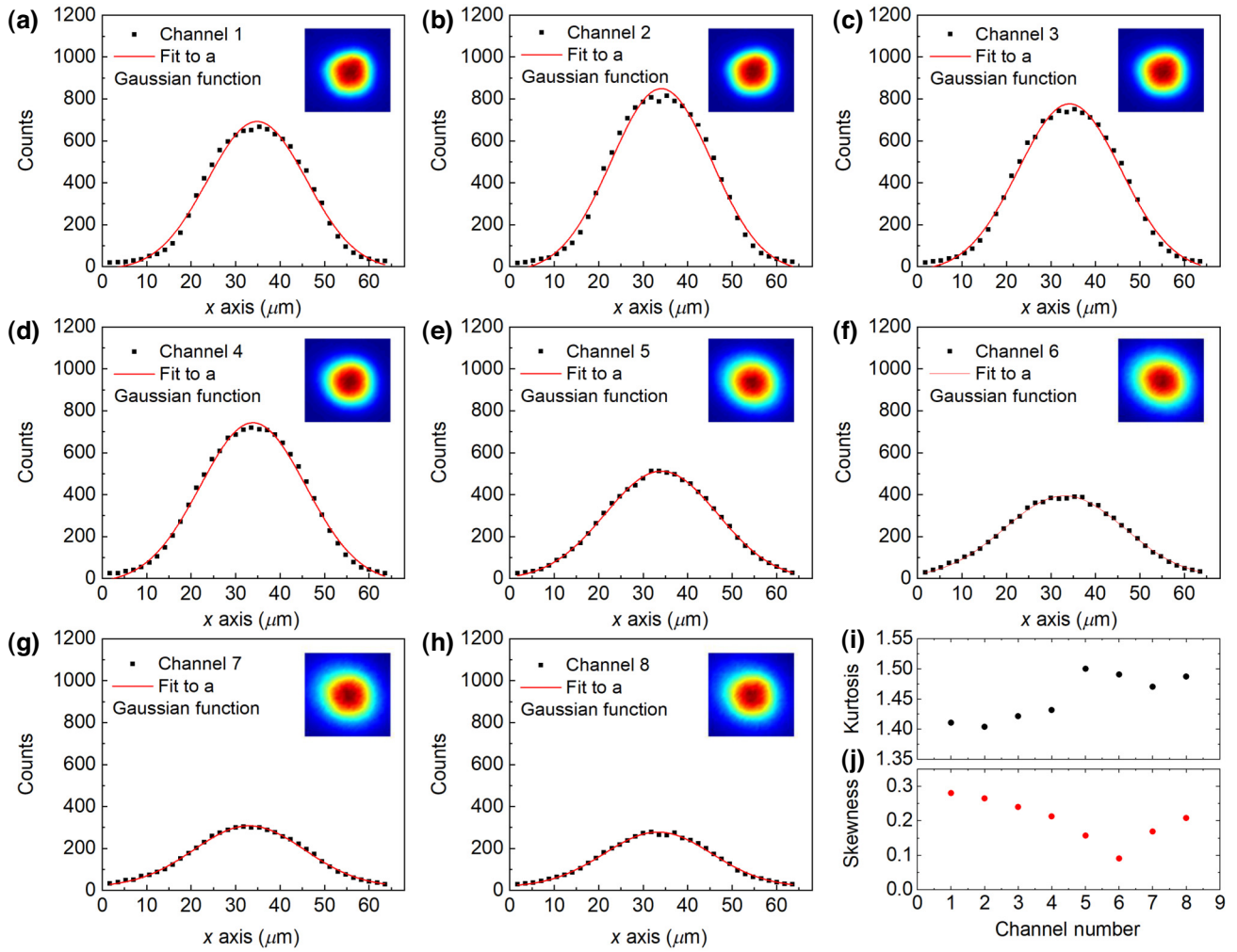


FIG. 4. (a)–(h) Line scans (black dots) from thermal images of a laser-irradiated Ti-6Al-4V surface, taken along the x axis at $y = 31.8 \mu\text{m}$ for eight different channels. The red lines are fits to a Gaussian function. The raw thermal images in the insets are mapped over an area of $63.6 \times 63.6 \mu\text{m}^2$. The color scale indicates the camera pixel counts normalized to a range of 0 (blue) to 1000 (red). The image is obtained by focusing the laser beam down to a diameter of $50 \mu\text{m}$ with an average power of 175 mW, a pulse width of $0.8 \mu\text{s}$, and a repetition rate of 1 kHz. (i),(j) The kurtosis (i) and skewness (j) of the line scans are plotted as a function of the channel number for the thermal profiles shown in (a)–(h). The kurtosis of a Gaussian distribution is 3. A kurtosis lower than 3 indicates that the data have light tails relative to a Gaussian distribution. The skewness of a Gaussian distribution is zero. A positive skewness indicates that the right tail of the data is long relative to the left tail.

by around 3 times to approximately 0.12, corresponding to temperatures ranging from 2100 to 2600 K. Outside of the expected melt-pool region, ε_{ave} becomes almost constant, such that $\varepsilon_{\text{ave}} \approx 0.135$ for $T < 2000\text{--}2100$ K. We find that ε_{ave} displays a strong dependence on temperature adjacent to the expected liquid-solid boundary, consistent with prior literature results [18].

To compare our extracted wavelength-dependent emissivity with a value obtained without making any assumptions regarding the dependence of the emissivity [20], we plot the normalized emissivity $\varepsilon(\lambda)/\varepsilon(544 \text{ nm})$ at $T \sim 1950$ K for two samples irradiated with the same laser power and the same beam diameter in Fig. 8. As the absolute magnitude of the emitted radiation depends

on the surface roughness [22], the degree of oxidation [23], and the turbulence in the liquid [24], which may vary from sample to sample, we focus on the wavelength dependence of the normalized emissivity here. Figures 8 (a) and 8(c) show the measured thermal radiance (black squares) fitted with Eqs. (1) and (4) for sample 1 and sample 2, respectively. The extracted normalized emissivity is in good agreement with the reported wavelength-dependent emissivity at $T = 1942$ K [Figs. 8(b) and 8(d)]. These results lead us to conclude that our hyperspectral imaging technique is able to quantify the wavelength dependence of the emissivity during laser-metal interaction and give an accurate evaluation of the temperature.

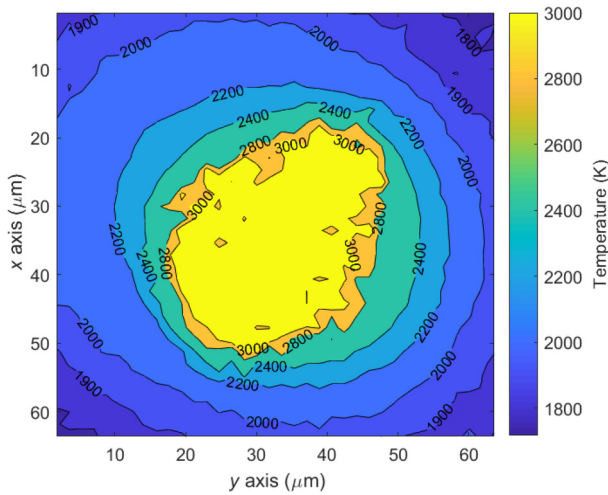


FIG. 5. Temperature-profile measurements during laser heating, obtained by the hyperspectral-camera-based method. The laser parameters are the same as in Fig. 4.

C. Time-resolved temperature profile

In addition to snapshots of thermal images, the hyperspectral camera captures time-dependent 2D temperature profiles of the laser-heated surface with a 60-Hz sampling rate and a 16.61-ms exposure time (t_{ex}). Figure 9 shows the measured temporal evolution of the surface temperature, $T(x, y, t)$, when the surface is irradiated with a pulsed laser beam. The starting time $t = 0$ is chosen to be a moment when the signal is strong enough to allow us to extract a temperature response. Early in the heating process, most of the area within the laser-beam diameter shows a time-averaged temperature below the melting temperature $T \sim 1900$ K. As time progresses, the maximum temperature steadily increases and quickly saturates the camera

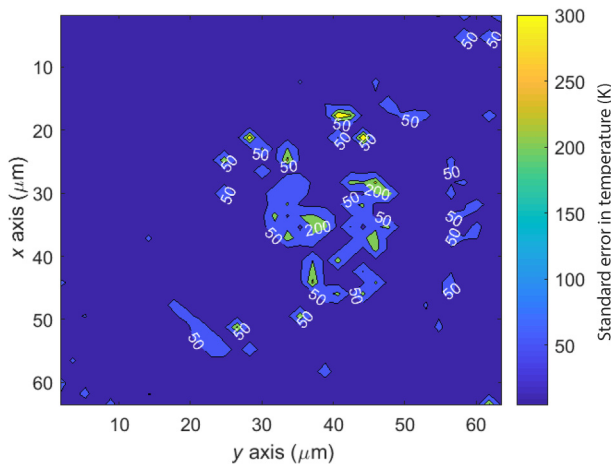


FIG. 6. Profile of the standard error in the temperature for the temperature plot shown in Fig. 5. The laser parameters are the same as in Fig. 4.

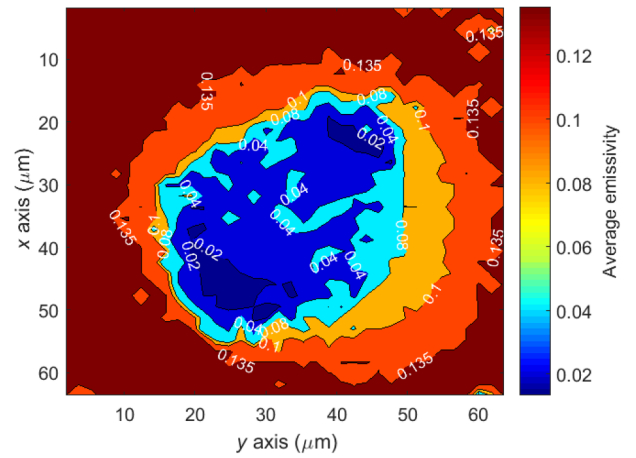


FIG. 7. Emissivity profile during laser heating. The laser parameters are the same as in Fig. 4.

sensor at $t = 133.6$ ms. The peak temperature rises by more than 600 K in the first 84 ms, followed by a slower rise of 100 K over the next 34 ms. Moreover, the thermal contour line at the melting point $T \sim 1900$ K expands rapidly from half of the beam diameter to 1.2 times the beam diameter over a short 130-ms laser exposure. However, due to the time-resolution limit of the camera and the nature of the signal averaging over the exposure time, the temperature evolution revealed by these measurements should be regarded as a time-averaged result within a 16.61-ms integration time. We will discuss this in detail in the simulation analysis below.

V. DISCUSSION

A. Thermal modeling of laser-heated Ti-6Al-4V

To provide points of reference for our experimental measurements and insight into the observed thermal trends, numerical calculations of pulsed-laser heating of Ti-6Al-4V are performed. The nonlinear 2D heat-flow equation

$$\rho C_p \frac{\partial T}{\partial t} = \nabla(k \nabla T) + Q \quad (5)$$

is solved, where t is the time and ρ , C_p , and k are the density, specific heat capacity, and thermal conductivity, respectively, of the metal. The heat-source term Q in the metal due to a Gaussian beam is taken as

$$Q(r, z, t) = \left[\frac{\alpha(1 - R_\lambda)P(t)}{\pi r_0^2} \right] \exp\left(-\alpha z - \frac{r^2}{r_0^2}\right), \quad (6)$$

where $P(t)$ is the incident laser power, r_0 is the $1/e$ Gaussian radius, and α and R_λ are the absorption coefficient and reflectivity, respectively, of the metal at an incident wavelength λ . z denotes the (vertical) direction parallel to the beam, and r the radial direction normal to the beam.

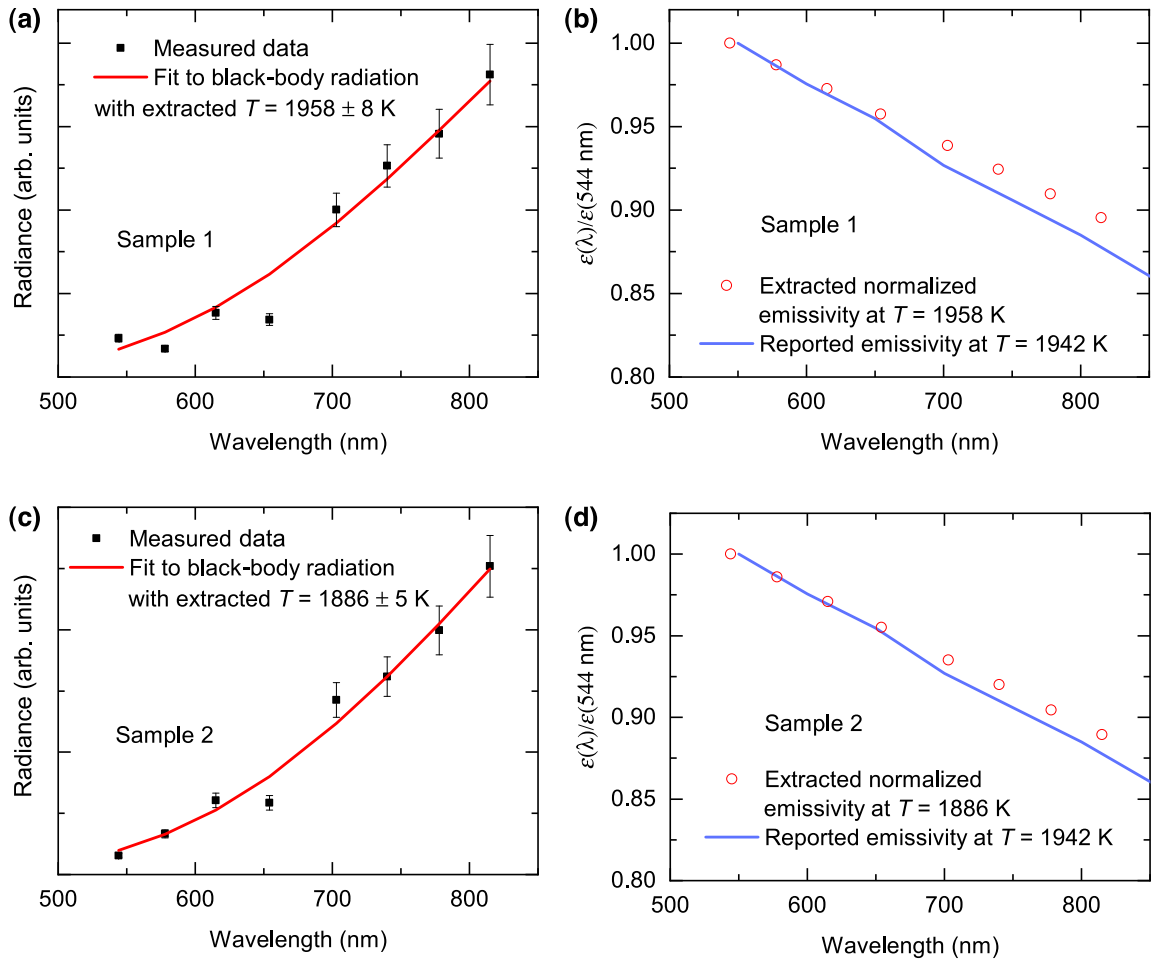


FIG. 8. (a),(c) Measured and calculated thermal response in a single pixel group for sample 1 (a) and sample 2 (c). The error bars indicate the estimated 10% error in the radiance measurement. The experimental data are fitted using Eq. (1). The extracted normalized emissivity (red circles) is compared with the reported value (blue line) [20] in (b),(d) for samples 1 and 2, respectively. The temperature in Ref. [20] was measured using immersion thermocouples in an induction-heated metal melt.

An estimate of the expected temperature variation on the metal surface with each early-time pulse cycle can be obtained from an analytic solution for a single rectangular pulse-decay cycle with a spatially uniform surface source ($\alpha \rightarrow \infty$) and conductive volumetric cooling [29]. For a pulse duration t_p and cycle duration t_0 , the maximum and minimum surface temperatures are (see Appendix A)

$$T(t = t_p) = \frac{2I_{\text{abs}}}{k} \sqrt{\frac{Dt_p}{\pi}} + T_0 \quad (7)$$

and

$$T(t = t_0) = \frac{2I_{\text{abs}}}{k} \sqrt{\frac{D}{\pi}} [\sqrt{t_0} - \sqrt{t_0 - t_p}] + T_0, \quad (8)$$

respectively, where I_{abs} is the absorbed laser power density, $D = k/\rho C_p$ is the thermal diffusivity, and T_0 is the initial temperature of the environment. Substituting the parameter values for Ti-6Al-4V at $T \approx T_m$ ($D = 7 \times 10^{-6} \text{ m}^2/\text{s}$, $k =$

30 W/m K ; see Table I) and $t_0 = 1 \text{ ms}$, $t_p = 0.8 \mu\text{s}$, and $I_{\text{abs}} = (1 - R_\lambda)P_0/\pi r_0^2 \approx 5 \times 10^{10} \text{ W/m}^2$ gives $T(t_p) \approx 4743 \text{ K}$ and $T(t_0) \approx 356 \text{ K}$ for $P_0 = 175 \text{ mW} \times t_0/t_p = 220 \text{ W}$. This indicates that the temperature variations at the beam center should be large enough to induce local melting (and potentially vaporization; $T_b = 3563 \text{ K}$) and freezing during each early-time laser-pulse cycle (i.e., transient or periodic rather than steady-state melt pools).

Full numerical solutions of Eq. (6) permit more detailed analysis. In the numerical calculations, the temperature dependences of the material properties of Ti-6Al-4V are incorporated as specified in Table I. A laser radius $r_0 = 25 \mu\text{m}$ is used, and the pulsed laser power $P(t)$ is approximated as $P_0 \sum_{n=0}^{\infty} \Pi[(t - nt_0)/t_p - 1/2]$, a periodic rectangular function with period $t_0 = 1 \text{ ms}$, pulse width $t_p = 0.8 \mu\text{s}$, and magnitude $P_0 = 220 \text{ W}$, all equivalent to the experimental values. The assumptions made in this model are outlined in Appendix B.

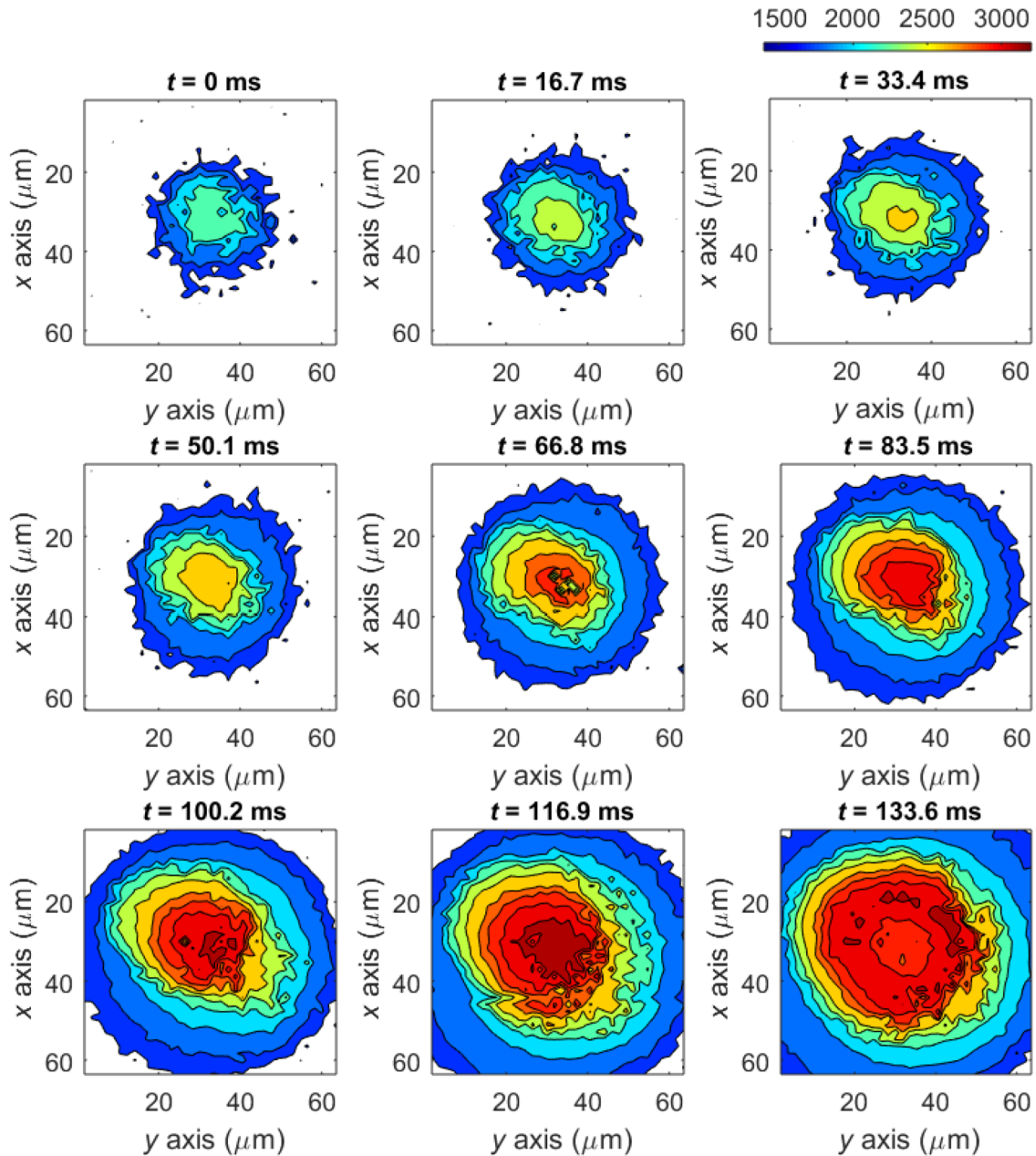


FIG. 9. Temporal evolution of temperature profile of laser-heated Ti-6Al-4V metal plate measured with the hyperspectral camera. The color bar represents the calculated temperature in units of kelvin.

Representative numerical results are shown in Fig. 10. A melt pool of diameter 30–50 μm and depth 10–20 μm quickly forms under the beam, within 1–10 μs . However, after each pulse, the rapid rate of thermal conduction within the metal leads to a large decrease in temperature, such that the maximum surface temperature varies by several thousand kelvin in each laser cycle [Fig. 10(b)]. The surface temperature at the beam center oscillates between approximately 5100 K and approximately 430 K during the early-time pulse-decay cycles, in good agreement with the analytic estimates above. A melt pool thus forms and

fully solidifies in each cycle (assuming that the solidification kinetics are sufficiently rapid, requiring a feasible average solidification velocity of approximately 2 cm/s or less), as anticipated.

The simulation results, including the large temperature oscillations, are largely consistent with our experimental measurements once the detector exposure time t_{ex} and the measurement procedure are taken into account. We simulate the experimental measurement procedure within our numerical calculations by first, for each numerical time interval, converting each local surface temperature to eight

TABLE I. Material parameters of Ti-6Al-4V used in numerical calculations. All temperatures are in units of kelvin. $R_{685 \text{ nm}}$ data are used because the reported $R_{1070 \text{ nm}}$ values [31] are laser-power- and scan-speed-dependent (rather than temperature-dependent and stationary) and do not distinguish between liquid and solid. This replacement does not significantly alter our results, as the magnitudes ($R_{1070 \text{ nm}} \approx 0.3\text{--}0.7$) are similar at these two wavelengths.

Physical property	Value	Reference
Melting temperature T_m (K)	1928	[27]
Boiling temperature T_b (K)	3563	[27]
Density ρ (kg/m ³)	$4420/(7.67 \times 10^{-5}T + 0.9743)$	[27]
Specific heat capacity C_p (J/kg K)	$757 (T \leq T_m)$ $1126 (T > T_m)$	[27]
Thermal conductivity k (W/m K)	$0.0146T - 0.32 (T \leq 1713 \text{ K})$ $0.0183T - 6.66 (T > 1713 \text{ K})$	[27]
Absorption coefficient α (m ⁻¹)	7×10^7 (Ti)	[28]
Reflectivity $R_{685 \text{ nm}}$	$0.4 (T \leq T_m)$ $0.6 (T > T_m)$	[27]

radiance intensities I_{λ_i} ($i = 1, \dots, 8$) using Eq. (1). Then all eight I_{λ_i} for each location are averaged over a time interval $t_{\text{ex}} = 16.61 \text{ ms}$ and converted to the corresponding “measured” temperature \tilde{T} using Eq. (1). This procedure highlights the fact that each experimentally measured temperature is a highly nonlinear average of the local temperature over the camera exposure time. The nonlinearity of

Eq. (1) applies much greater weight to higher temperature values.

The computed magnitudes of \tilde{T} (see Fig. 10) are in good agreement with the experimental measurements, with the exception of the absence of the consistently measured increase of approximately 500–1000 K between the initial signal detection and detector saturation [magenta

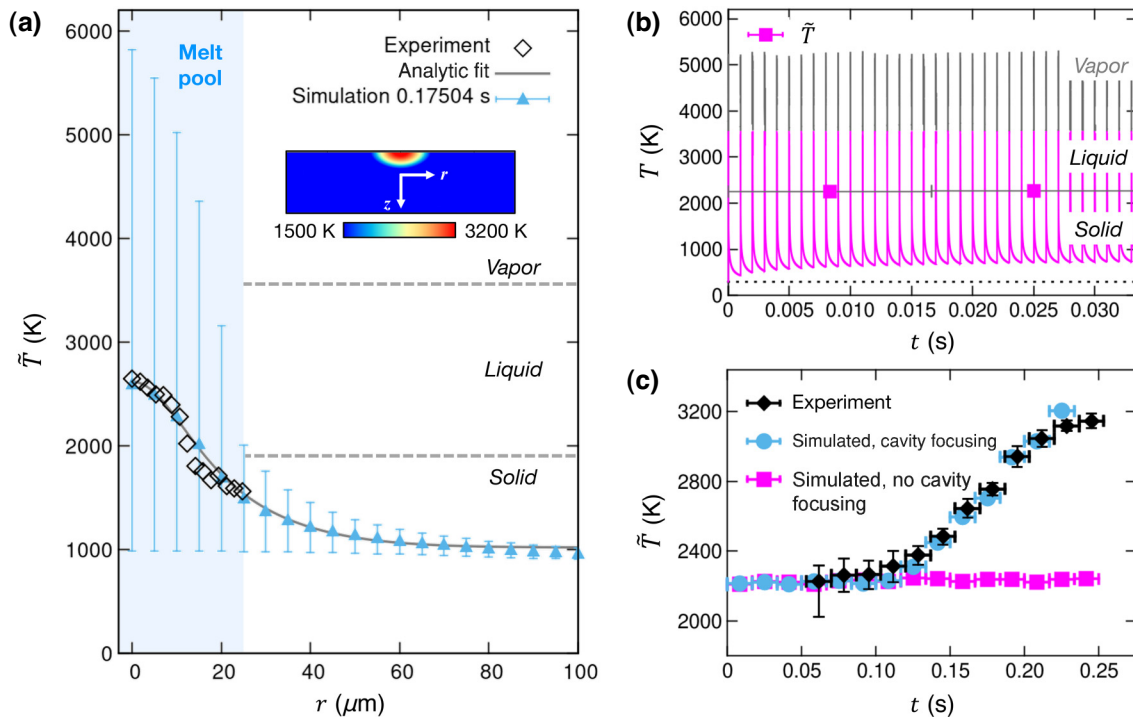


FIG. 10. Thermal modeling of laser-heated Ti-6Al-4V. (a) Computed \tilde{T} profile (with cavity focusing). The vertical bars indicate the magnitude of the oscillation of the maximum $T(r, z)$ over t_{ex} , and the gray line is a fit of the simulation data to the form of the analytic Green’s-function solution presented in Appendix A. The inset shows a representative $T(r, z)$ profile over a $150 \times 40 \mu\text{m}^2$ region. (b) Large temporal oscillations in the surface temperature of the metal (magenta lines) and the vapor temperature (gray lines) at the beam center. The corresponding \tilde{T} ($t_{\text{ex}} = 16.61 \text{ ms}$) is also shown. (c) Experimentally measured and simulated \tilde{T} values without and with cavity focusing. The vertical experimental error bars (black) correspond to 95% confidence bounds.

points in Fig. 10(c)]. A thermal steady state with respect to volumetric diffusion is established rapidly in the simulations (in a time much less than 0.1 s), indicating that any additional heating over longer time scales results from some unconsidered form of heat focusing or trapping.

A potential source of this heat focusing is hole drilling or crater formation, which is observed in our experiments. This results from transport of mass (via, e.g., liquid spatter induced by Marangoni forces and recoil vapor pressure, vaporization, etc.) away from the melt-pool area during the high-energy laser pulse [31–33]. The altered geometry of the laser-metal interaction region enhances the thermal energy input, largely by enabling multiple reflections of laser radiation off the crater walls [33]. Such effects tend to self-amplify as the crater deepens, concentrating greater energy within the crater, increasing the effective absorptivity of the surface, and potentially leading to effective local laser intensities orders of magnitude larger than the applied intensity [30]. We qualitatively consider this effect by assuming that the crater grows with time such that the heat energy absorbed at the center of the beam, $Q(0, 0, t)$, increases after each pulse by $\beta t^2 Q(0, 0, 0)$. β is a constant that sets the time scale for crater growth; we treat this term as a fitting parameter. The results shown in Fig. 10(c) (blue data points) demonstrate that this effect can produce a rise in \bar{T} similar to that observed in the experiments, where the effective local laser intensity at the center of the melt pool becomes greater than the applied intensity by approximately 10 times or more.

We conclude that our measurement approach produces temperature values consistent with thermal-modeling results and that the experimentally observed increases by approximately 500–1000 K appear to be consistent with the effect of thermal focusing due to crater formation.

The experimental and computational work presented here paves the way to higher-accuracy temperature measurements of laser-processed material surfaces. As discussed, multiple physical effects occurring during processing can strongly affect surface temperatures, creating challenges to the community working on the modeling of laser welding and additive manufacturing via laser powder-bed fusion. Furthermore, changes in surface properties often drive complex solutions to the emissivity problem, often with less than ideal levels of accuracy. By using a compact multispectral filter and a careful calibration process, we can achieve high accuracy, good spatial resolution, and a scalable solution in terms of wavelength range and frame rate. Since most cutting-edge laser processes such as laser powder-bed fusion occur over characteristic time scales of microseconds, future work will be aimed at integrating the multispectral filter into a high-frame-rate camera such as the ones used in Refs. [9] and [17]. With that integration, we expect a breakthrough in accuracy, resolution, and speed associated with validation

data that can be used with high-fidelity models, leading to unprecedented prediction capabilities to improve process quality.

VI. CONCLUSIONS

This paper presents a method for measuring a 2D temperature profile of a Ti-6Al-4V surface during pulsed near-infrared laser irradiation. The spectral radiance emitted by the surface is captured with an eight-wavelength hyperspectral camera with a spatial resolution of 15.9 $\mu\text{m}/\text{pixel}$ and a maximum temporal resolution of 60 frames per second. The temperature and emissivity values are simultaneously estimated by fitting the measured spectral radiance to Planck’s law, assuming that the spectral emissivity decreases linearly with wavelength. The extracted spectral-emissivity value is in good agreement with reported emissivity values obtained without making any assumptions. Our results show that the temperature of a melt-pool surface can be determined with an accuracy of approximately 5%–10% when the melt pool is sustained over the detector exposure time t_{ex} . Thermal profiles that change significantly during t_{ex} , as our thermal-modeling results indicate is the case in the pulsed experiments, result in a highly nonlinear average of the local temperature over t_{ex} . Measurements under such circumstances should be interpreted accordingly. For future research directions, the hyperspectral imaging technology presented here can be used as a platform in connection with a high-speed camera system for *in situ* monitoring of the temperature distribution during laser metal processing, such as in laser welding, laser deposition, and metal additive manufacturing.

ACKNOWLEDGMENTS

The authors would like to thank Saad A. Khairallah and Clara Letitia for helpful discussions. This work was performed under the auspices of the U.S. Department of Energy at Lawrence Livermore National Laboratory under Contract No. DE-AC52-07NA27344. The project was supported by the Laboratory Directed Research and Development programs of LLNL (Grant No. 18-SI-003).

APPENDIX A

1. Analytic solution for a single thermal pulse-decay cycle with a uniform surface source and volumetric cooling

For a uniform surface heat source applied over a single rectangular pulse-decay cycle, the analytic solution for

conductive volumetric cooling is [29]

$$T(z, t) = \frac{2I_{\text{abs}}\sqrt{D}}{k} \left[\sqrt{t} \text{IERFC} \left(\frac{z}{2\sqrt{Dt}} \right) - H(t - t_p) \sqrt{t - t_p} \text{IERFC} \left(\frac{z}{2\sqrt{D(t - t_p)}} \right) \right] + T_0, \quad (\text{A1})$$

where I_{abs} is the absorbed laser power density, $D = k/\rho C_p$ is the thermal diffusivity, H is the Heaviside step function, IERFC is the inverse complementary error function, and T_0 is the initial temperature of the environment. The maximum and minimum surface temperatures $T(t_p)$ and $T(t_0)$, respectively, during the cycle are straightforwardly obtained by substituting $z = 0$ and $t = t_p$ or $t = t_0$ [see Eqs. (7) and (8)]. Accordingly, the surface temperature spans a range of magnitude

$$\Delta T_{\text{osc}} = T(0, t_p) - T(0, t_0) = \frac{2I_{\text{abs}}\sqrt{D}}{k} \left[\sqrt{t_p} - \sqrt{t_0} + \sqrt{t_0 - t_p} \right]. \quad (\text{A2})$$

A similar result for $T(t_p)$ is obtained for a Gaussian surface source,

$$T(t = t_p) = \frac{2I_{\text{abs}}r_0}{\sqrt{\pi k}} \tan^{-1} \left(\sqrt{\frac{4Dt_p}{r_0^2}} \right) + T_0. \quad (\text{A3})$$

This result is well approximated by the uniform-source result, Eq. (7), for $I_{\text{abs}} = (1 - R_\lambda)P_0/\pi r_0^2$ (as specified in the main text) and $t_p \ll r_0^2/4D$ (here, $r_0^2/4D \approx 22 \mu\text{s} \gg t_p = 0.8 \mu\text{s}$).

2. Analytic Green's-function solution for a continuous 2D Gaussian source and volumetric cooling

A time-dependent solution for the case of a continuous 2D Gaussian heat source $Q(r) = A \exp(-r^2/r_0^2)$, for comparison with the simulation results shown in Fig. 10(a), is [34]

$$T(r, t) = -\frac{Ar_0^2}{2k} \left[\text{EI} \left(1, \frac{r^2}{2r_0^2} \right) - \text{EI} \left(1, \frac{r^2}{2r_0^2 + 4Dt} \right) \right] + T_0, \quad (\text{A4})$$

where $\text{EI}(1, x) = \int_1^\infty t^{-1} e^{-xt} dt$ is the exponential integral.

APPENDIX B

1. Assumptions in the simulation

Our description assumes that the metal surface remains unoxidized, and it does not include the (unknown) temperature dependence of the reflectivity or emissivity. The

effects of radiative cooling and of latent heat during melting and solidification are found to be minimal and are thus removed for simplicity. Convection and convective cooling are neglected due to the orders-of-magnitude larger conduction term in the heat transport equation. Since our calculations indicate that a small amount of metal is heated above the boiling temperature T_b of Ti-6Al-4V during each laser pulse, a simple scheme is constructed to approximate the net thermal effect of vaporization-condensation processes. This approximation scheme applies to a small fraction of the total thermal input and does not have a major effect on the results. We assume that metal regions heated above T_b vaporize rapidly (within tens to hundreds of nanoseconds), remain localized above the metal surface, exhibit a small thermal conductivity (one-tenth that of the solid metal), and do not absorb additional thermal energy from the laser beam. When the vapor cools below T_b after the pulse, it is reintegrated into the slab as liquid metal (condensation is assumed to occur within tens to hundreds of nanoseconds), which subsequently cools below T_m and resolidifies. Transport of some vaporized metal away from the melt-pool region rather than 100% recondensation into the melt pool (a mass loss of vapor of approximately 82% has been predicted under steady-state conditions [35]) would lead to some degree of evaporative cooling. However, the mass vaporized under the conditions considered here is small, and the associated effects can reasonably be neglected.

To account for the effect of the vapor phase on the measured temperatures, the local irradiance of the vapor is added to that of the local metal surface in the computation of \tilde{T} . The radiance associated with the matter at T_{vapor} , computed using Eq. (1), is added to that associated with the liquid or solid surface directly below. T_{vapor} is taken as the average temperature of all vapor phase present at a given radial position r . Since T_{vapor} is exponentiated in Eq. (1), it can have a significant effect on \tilde{T} ; we observe an upward shift of up to approximately 700 K relative to the values determined from the liquid-solid surface temperature alone. However, the details of the treatment of the vapor phase (retention versus loss of vapor, approximation as superheated liquid rather than vapor, etc.) have little overall effect on \tilde{T} . This is mainly due to the short duration of the laser pulse (a small t_p/t_0), the correspondingly short lifespan of the vapor, and the small total amount of vapor.

-
- [1] T. Wohlers and T. Caffrey, Additive manufacturing: Going mainstream, *Manuf. Eng.* **150**, 67 (2013).
 - [2] T. T. Wohlers, Wohlers Report 2016: 3D Printing and Additive Manufacturing State of the Industry Annual Worldwide Progress Report, Wohlers Associates, Inc., Fort Collins, CO (2016).

- [3] A. Goulas, J. G. P. Binner, R. A. Harris, and R. J. Friel, Assessing extraterrestrial regolith material simulants for in-situ resource utilisation based 3D printing, *Appl. Mater. Today* **6**, 54 (2017).
- [4] T. Vilaro, C. Colin, and J. D. Bartout, As-fabricated and heat-treated microstructures of the Ti-6Al-4V alloy processed by selective laser melting, *Metall. Mater. Trans. A* **42**, 3190 (2011).
- [5] H. K. Rafi, N. V. Karthik, H. Gong, T. L. Starr, and B. E. Stucker, Microstructures and mechanical properties of Ti6Al4V parts fabricated by selective laser melting and electron beam melting, *J. Mater. Eng. Perform.* **22**, 3872 (2013).
- [6] B. Song, S. J. Dong, S. H. Deng, H. L. Liao, and C. Coddet, Microstructure and tensile properties of iron parts fabricated by selective laser melting, *Opt. Laser Technol.* **56**, 451 (2014).
- [7] M. M. Kirka, P. Nandwana, Y. Lee, and R. R. Dehoff, Solidification and solid-state transformation sciences in metals additive manufacturing, *Scr. Mater.* **135**, 130 (2017).
- [8] T. T. Roehling, S. S. Q. Wu, S. A. Khairallah, J. D. Roehling, S. S. Soezeri, M. F. Crumb, and M. J. Matthews, Modulating laser intensity profile ellipticity for microstructural control during metal additive manufacturing, *Acta Mater.* **128**, 197 (2017).
- [9] M. J. Matthews, G. Guss, S. A. Khairallah, A. M. Rubenchik, P. J. Depond, and W. E. King, Denudation of metal powder layers in laser powder bed fusion processes, *Acta Mater.* **114**, 33 (2016).
- [10] G. Tapia and A. Elwany, A review on process monitoring and control in metal-based additive manufacturing, *J. Manuf. Sci. Eng.* **136**, 060801 (2014).
- [11] A. P. Tadamalle, Review of real-time temperature measurement for process monitoring of laser conduction welding, *Eng. Sci. Technol. An Int. J.* **2**, 946 (2012).
- [12] B. Müller and U. Renz, Development of a fast fiber-optic two-color pyrometer for the temperature measurement of surfaces with varying emissivities, *Rev. Sci. Instrum.* **72**, 3366 (2001).
- [13] J. M. Densmore, B. E. Homan, M. M. Biss, and K. L. McNesby, High-speed two-camera imaging pyrometer for mapping fireball temperatures, *Appl. Opt.* **50**, 6267 (2011).
- [14] M. Müller, R. Fabbro, H. El-Rabii, and K. Hirano, Temperature measurement of laser heated metals in highly oxidizing environment using 2D single-band and spectral pyrometry, *J. Laser Appl.* **24**, 022006 (2012).
- [15] W. P. Bassett and D. D. Dlott, 32-channel pyrometer with high dynamic range for studies of shocked nanothermites, *AIP Conf. Proc.* **1793**, 060012 (2017).
- [16] D. J. Dagela, G. D. Grossetetea, D. O. MacCalluma, and S. P. Koreyb, Four-color imaging pyrometer for mapping temperatures of laser based metal processes, *Proc. SPIE 9861, Thermosense: Therm. Infrared Appl. XXXVIII* **9861**, 986103 (2016).
- [17] P. A. Hooper, Melt pool temperature and cooling rates in laser powder bed fusion, *Addit. Manuf.* **17**, 548 (2018).
- [18] W. Devesse, D. D. Baere, and P. Guillaume, High resolution temperature measurement of liquid stainless steel using hyperspectral imaging, *Sensors* **17**, 91 (2017).
- [19] D. P. DeWitt and J. C. Richmond, in *Theory and Practice of Radiation Thermometry* (John Wiley & Sons, New York, NY, 1988).
- [20] R. Felice, Pyrometry for liquid metals, *Adv. Mater. Processes* July, 31 (2008).
- [21] X. He, P. W. Fuerschbach, and T. DeRoy, Heat transfer and fluid flow during laser spot welding of 304 stainless steel, *J. Phys. D: Appl. Phys.* **36**, 1388 (2003).
- [22] C.-D. Wen and I. Mudawar, Emissivity characteristics of roughened aluminum alloy surfaces and assessment of multispectral radiation thermometry (MRT) emissivity models, *Int. J. Heat Mass Transf.* **47**, 3591 (2004).
- [23] J. L. King, H. Jo, R. Tirawat, K. Blomstrand, and K. Sridharan, Effects of surface roughness, oxidation, and temperature on the emissivity of reactor pressure vessel alloys, *Nucl. Tech.* **200**, 1 (2017).
- [24] D. M. Olinger, J. V. Gray, and R. A. Felice, in *Investment Casting Institute 55th Technical Conference and Expo.* Oct. 14–17, Cleveland, Ohio (2007).
- [25] Z. Fan and F. Liou, in *Titanium Alloys—Towards Achieving Enhanced Properties for Diversified Applications*, edited by A. K. M. Nurul Amin (IntechOpen, London, United Kingdom, 2012), p. 1.
- [26] T. Lips and B. Fritsche, A comparison of commonly used re-entry analysis tools, *Acta Astronautica* **57**, 312 (2005).
- [27] M. Boivineau, C. Cagran, D. Doytier, V. Eyraud, M-H Nadal, B. Wilthan, and G. Pottlacher, Thermophysical properties of solid and liquid Ti-6Al-4V (TA6V) alloy, *Internat. J. Thermophys.* **27**, 507 (2006).
- [28] P. B. Johnson and R. W. Christy, Optical constants of transition metals: Ti, V, Cr, Mn, Fe, Co, Ni, and Pd, *Phys. Rev. B* **9**, 5056 (1974).
- [29] M. v. Allmen, *Laser-Beam Interactions with Materials: Physical Principles and Applications* (Springer-Verlag, Berlin Heidelberg, New York, 1987).
- [30] H. Ki, P. S. Mohanty, and J. Mazumder, Multiple reflection and its influence on keyhole evolution, *J. Laser Appl.* **14**, 39 (2002).
- [31] B. J. Simonds, J. Sowards, J. Hadler, E. Pfeif, B. Wilthan, J. Tanner, C. Harris, P. Williams, and J. Lehman, Time-Resolved Absorptance and Melt Pool Dynamics during Intense Laser Irradiation of a Metal, *Phys. Rev. Appl.* **10**, 044061 (2018).
- [32] J. Ye, S. A. Khairallah, A. M. Rubenchik, M. F. Crumb, G. Guss, J. Belak, and M. J. Matthews, Energy coupling mechanisms and scaling behavior associated with laser powder bed fusion additive manufacturing, *Adv. Eng. Mater.* **21**, 1900185 (2019).
- [33] D. Shah and A. N. Volkov, Simulations of deep drilling of metals by continuous wave lasers using combined smoothed particle hydrodynamics and ray-tracing methods, *Appl. Phys. A* **126**, 82 (2020).
- [34] T. Antonakakis, C. Maglioni, and V. Vlachoudis, Closed form solutions of the heat diffusion equation with a Gaussian source, *Int. J. Heat Mass Transf.* **62**, 314 (2013).
- [35] S. I. Anisimov and V. A. Khokhlov, *Instabilities in Laser-Matter Interaction* (CRC Press, Boca Raton, Florida, 1995).